Surface reconstruction of Au(001): High-resolution real-space and reciprocal-space inspection

R. Hammer,[1] A. Sander,[1] S. Förster,[1] M. Kiel,[1] K. Meinel,[1] and W. Widdra[1,2]
[1]*Institute of Physics, Martin-Luther-Universität Halle-Wittenberg, D-06099 Halle, Germany*
[2]*Max-Planck Institut für Mikrostrukturphysik, D-06120 Halle, Germany*
(Received 12 June 2014; revised manuscript received 6 July 2014; published 28 July 2014)

The hexagonal reconstruction of Au(001) has been a model system for the understanding of complex metal surface reconstructions, and it has been intensively studied over almost five decades. Nevertheless, details of the reconstruction regarding the top layer to substrate matching and alignment are not unambiguously identified due to restricted resolution of previously available analytical tools as well as nonuniform sample quality. We therefore quantitatively reinvestigated the system by applying high-resolution real-space and reciprocal-space inspection using scanning tunneling microscopy and spot profile analysis low-energy electron diffraction in analyzing a high-quality Au(001) sample. We show that the Au(001) reconstruction consists of two rotational domains of a commensurate $c(28 \times 48)$ superstructure. It results from a Moiré-like buckling of a quasihexagonal top layer which is characterized by lattice vectors having a length of $0.9655a$ and $0.9581a$, respectively, where a is the interatomic distance of Au(001). The former vector runs exactly along [110] or [−110], whereas the latter one deviates by 59.75° from those directions. Ar^+ ion bombardment at elevated temperatures induces a rotation of the top layers up to angles of ±0.83°. Sample annealing yields a turning back into the initial top layer alignment. Rotation and reorientation proceeds continuously, i.e. all angles between 0 and ±0.83° are observed. Using simple hard sphere models, the main characteristics of the reconstruction are explained. This includes even structural details of the reconstruction at step edges for nonrotated and rotated quasihexagonal top layers.

DOI: 10.1103/PhysRevB.90.035446 PACS number(s): 68.35.−p, 68.37.−d

I. INTRODUCTION

Gold as a noble metal has fascinated mankind for millennia due to its uniqueness and rarity. However, today's interest is not restricted to jewelry and monetary aspects only. There are fascinating new industrial and scientific implementations, e.g. in catalytic [1,2] and electrochemical processes [3–5], in microelectronics [6], formation of self-assembled nanostructures, such as magnetic dots [7,8], organic molecules [9,10], metal oxides [11–14], as well as kinetics and dynamics of surface processes [15–20]. Within these applications, texture and quality of the given Au surface are essential for the performance. Specifically for Au, a strong tendency for surface reconstructions has to be taken into account. All low index surfaces of Au display atomic structures that deviate from corresponding bulk arrangements. Au(111) shows an uniaxial reconstruction yielding a surface modulation known as herring bone structure [21,22]. Au(011) displays a missing row reconstruction that induces highly corrugated (1×2) or (1×3) surfaces [23,24]. Au(001), on the other hand, develops a contracted quasihexagonal (hex) top layer on the (1×1) square lattice where close packed atomic rows are aligned along [110] or [−110] directions. Hence, two hex layer domains are formed with a mutual twist of 90° displaying a Moiré-like buckling due to the structural difference to the square lattice Au(001) substrate. This results in a complex low-energy electron diffraction (LEED) pattern, which was interpreted by Fedak and Gjostein in 1966 [25] as a (1×5) superstructure and one year later as a (5×20) superstructure [26]. Besides the Si(111)-(7×7) [27–29], the Au(001)-hex structure belongs to the first scientifically accepted examples of complex surface reconstruction. Initially suspected to be impurity induced [30], it was soon identified as an intrinsic surface modification [31,32], which is established not only *in vacuo* but also in solutions under electrochemical environment [3,5] and during homoepitaxial growth [18,20]. The (5×20) designation of the Au(001) reconstruction is, however, only an approximation to the real surface structure. Reflection high-energy electron diffraction (RHEED) [33,34] and He diffraction [35] as well as reinspections by LEED [36] yield that a (5×20) ordering could not explain all details of the diffraction pattern. Moreover, for stepped samples, a slight rotation of the hex layer by 0.7° was observed which has been characterized by a $\begin{pmatrix} 14 & 1 \\ -1 & 5 \end{pmatrix}$ structure [34]. Based on refined LEED measurement of Wendelken and Zehner [37], Van Hove *et al.* [21] deduced that the Au(001) reconstruction is more realistically described by a $c(28 \times 68)$ structure, whereas also an incommensurate structure could not be excluded. In the first scanning tunneling microscopy (STM) measurements of Au(001) by Binnig *et al.* [38] a $c(26 \times 48)$ superstructure was locally detected. They found also indications of a slight rotation of the hex layer resulting in a $\begin{pmatrix} X & 0 \\ Z & Y \end{pmatrix}$ reconstruction where $X = 24 \pm 3$, $Y = 48$ or 43, and $-5 < Z < 0$. From transmission electron microscope studies of thin Au crystallites, Yamazaki *et al.* [39] deduced a (5×28) superstructure and a hex layer rotation of 0.5°–0.7° depending on local step geometry. Using the high resolution of spot profile analysis low-energy electron diffraction (SPA-LEED), Liew and Wang [40] confirmed the (5×28) reconstruction for samples with high step density. In reflection electron microscopy studies performed by Wang *et al.* [41,42], domains of some of the reported different surface reconstructions were observed simultaneously in coexistence. In addition, they report on specific $\begin{pmatrix} 27 & 2 \\ -2 & 5 \end{pmatrix}$ and $\begin{pmatrix} 83 & 1 \\ -1 & 72 \end{pmatrix}$ superstructures formed by twisted hex layer areas. Gibbs *et al.* [43] deduced from glancing incidence x-ray diffraction studies that the hex layer locally displays commensurate regions that are separated by incommensurate domain walls running along [110]. In the temperature region between 300 and 970 K, it coexists with

rotated domains of the hex layer displaying a rotation angle of $\pm 0.81°$. In recent high-resolution STM measurements of the nonrotated Au(001)-hex, de la Figuera *et al.* [44] revealed a (5×23) reconstruction whereas Trembulowicz *et al.* [20] observed a (5×29) structure for temperatures below 100 K, similar to that reported for the reconstruction of Pt(001) [45].

The experimental work has been accompanied by several theoretical studies [46–49], which could qualitatively explain some reconstruction features. As most striking result, Takeuchi *et al.* [48] and Havu *et al.* [49] showed by density functional theory (DFT) calculations that a relativistically enhanced *d-d* hybridization has to be included for explaining the reconstruction. For freestanding Au(111) planes, it yields a considerable lowering of the energy if they are contracted in the same form as the Au(001)-hex layer. The theoretical modeling of the Au(001) surface is highly demanding due to its large unit cell. Therefore, Havu *et al.* [49] used $(5 \times N)$ supercells as approximants with N around 20 and more than 100 atoms per layer to obtain qualitative reconstruction trends. However, the even larger real structure with more than 600 atoms per layer (as we will present below) is still beyond the computational possibilities of first principle descriptions.

Hence, the strange situation remains that, for a well-known reconstruction system continuously studied over almost 50 years, no clear and undisputed structural model has been determined up to now. One obstacle for a clear structure determination is the fact that the reconstruction significantly depends on the crystal quality and the surface perfection. Several studies [5,34,39,50,51] revealed that the Au(001) reconstruction strongly depends on surface steps and terrace widths, respectively. Also the influence of dislocations [44,52,53] and ion bombardment induced surface defects [54] have been demonstrated. Moreover, there are the limitations of the available techniques. Scanning tunneling microscopy and transmission electron microscopy (TEM), for example, are of high-resolving power but can deliver only local structural information. Conventional LEED, on the other hand, yields large-area results but its structural resolution is restricted due to the relatively low transfer width of about 10 nm. This is insufficient for a quantitative study of structures having significantly larger unit cells. Application of SPA-LEED would be a promising alternative since, here, the transfer width is in the range of 200 nm [55]. As a matter of fact, there already exists a SPA-LEED study of the Au(001) reconstruction [40]. Unfortunately, a Au crystal of relatively high step density was used (mean terrace width 10–15 nm), which is not representative for a perfect sample.

In this paper, the Au(001) reconstruction is reexamined by using a high-quality Au(001) crystal and by combining the high-resolving power of SPA-LEED and room-temperature as well as low-temperature STM. It was additionally motivated by the open issue whether the hex reconstruction layer may take a commensurate registry to the (1×1) square lattice substrate or whether it is strictly incommensurate. A further goal was the clarification under which conditions and in which way a rotation of the hex layer occurs. Finally, the interaction of the reconstruction layer and atomic surface steps was of interest.

It will be shown in this paper that, on large defect free terraces, the hex layer obeys a Moiré-like $c(28 \times 48)$ superstructure, which is in commensurate registry with the (1×1) square lattice of the Au(001) substrate. Rotation of the hex layer is attained by high-temperature sputtering of the sample. Rotation proceeds continuously from $0°$ to $\pm 0.83°$ and is continuously turned back again by annealing at temperatures around 900 K. Employing a Moiré approach, the diffraction patterns of the nonrotated as well as the rotated reconstruction structure have been simulated reproducing well the observed spot intensity distributions. Using a hard sphere model of the $c(28 \times 48)$ reconstruction for interpreting the STM results, a detailed description of the interplay between steps and reconstruction features for both nonrotated and rotated hex structures has been attained.

II. EXPERIMENT

The experiments have been performed in three ultrahigh vacuum (UHV) systems (base pressure 1×10^{-10} mbar). One is equipped with a cylindrical mirror analyzer for Auger electron spectroscopy (AES), a home-built room temperature STM, and a commercial electron optic (Omicron) for SPA-LEED. The second one contains conventional LEED (Omicron) and a home-built low-temperature STM operating with a commercial Konti cryostat (Cryovac) at 30 K. The third system holds conventional LEED (ErLEED) and a home-built variable-temperature STM. In all systems, the usual facilities for sample cleaning via Ar^+ sputtering and annealing have been established. In the investigations, a high-quality Au(001) crystal (Mateck) has been used. It was selected from several other samples (all with a miscut $<0.2°$) that show larger mosaic-like misorientations. The Au(001) crystal was cleaned *in situ* by cycles of 500 eV Ar^+ ion sputtering and annealing at temperatures of 800 K. Sputtering ions hit the sample at an angle of $45°$ with a current density of 3 μAcm^{-2}. For sample annealing, W filaments mounted behind the sample holders have been used for heating by radiation and electron bombardment. Surface cleanliness and structural perfection of the surface were checked by AES, STM, and LEED. The AES spectra show only the known characteristic Auger features of Au. In STM, usually large terraces (width several hundreds of nanometers) have been revealed with steps running prominently along [110]-like directions. Scanning tunneling microscopy and LEED reveal in best quality the signatures of the Au(001)-hex reconstruction. Transfer width of SPA-LEED was estimated to be better than 200 nm. Spot width (0.8% of Brillouin zone) remained constant for measurements ranging from 40 to 400 eV, which indicated that mosaiclike misorientations are smaller than $0.01°$. Rotation of the hex layer was achieved by Ar^+ ion bombardment at a temperature of 500 K. For attaining high-precision structure determination, the characteristic barrellike distortion of the SPA-LEED image [56] was corrected. For this calibration, we have used samples with a well-known structure and high density of diffraction spots. We prepared Si(111)-7×7 [29] samples, $BaTiO_3$(001) thin films on Pt(001) [57] displaying a series of oxygen vacancy induced orderings ranging from (2×2) up to $c(10 \times 10)$ and (10×10) variants, as well as TiO_2 layers on Pt(001) displaying (4×13) domains [58].

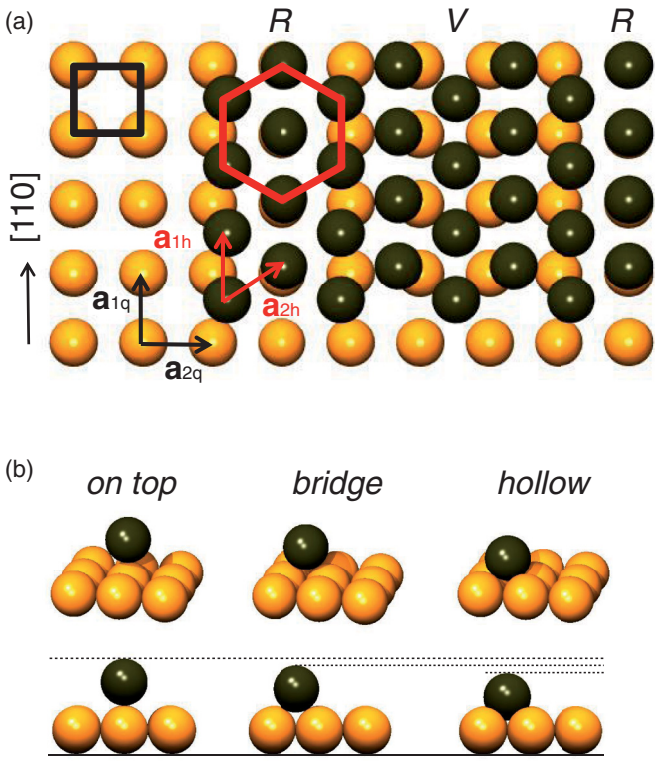

FIG. 1. (Color online) Hard sphere model of the nonrotated Au(001)-hex layer (atoms in black) in (a) top and (b) side views. Lattice vectors $\mathbf{a}_{1,2q}$ and $\mathbf{a}_{1,2h}$ of the Au(001) substrate square lattice (atoms in yellow) and the hex layer are drawn as black and red arrows, respectively. Due to the structural mismatch between the hex and the Au(001) substrate square lattice a characteristic row pattern along [110] is formed where the hex atoms reside either in top and bridge (R) or in hollow and bridge positions (V).

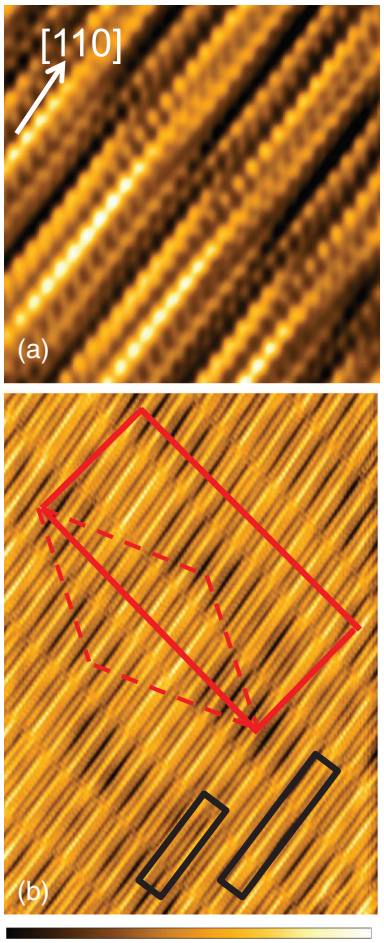

FIG. 2. (Color online) Atomically resolved STM images of the Au(001)-hex (500 pA, 1V) displaying the characteristic reconstruction rows along [110]. Image sizes (a) 5×5 nm^2 and (b) 24×34 nm^2. Black rectangles indicate (5×20) and (5×28) unit cells reported in literature. The real dimension of the unit cell present is sketched in red and correspond to a centered $c(2m \times 2n)$ structure. The color code for the apparent STM height between 0 and 60 pm is given at the bottom.

III. RESULTS AND DISCUSSIONS

A. The nonrotated Au(001)-hex

For a schematic real space visualization, a simplified hard sphere model of the Au(001) reconstruction is presented in Fig. 1. On the substrate (1×1) square lattice (lattice vectors $\mathbf{a}_{1,2q}$), a slightly compressed two-dimensional hex layer is present, which is characterized by the lattice vectors $\mathbf{a}_{1,h}$ and $\mathbf{a}_{2,h}$. Vector $\mathbf{a}_{1,h}$ runs along the [110] direction parallel to the close packed atomic rows of Au(001)-(1×1) and enclose with $\mathbf{a}_{2,h}$ the angle $\varphi \approx 60°$. The atoms of the hex layer reside in different heights over the Au(001)-(1×1) substrate as indicated for top, saddle, and hollow positions. As a consequence, the reconstruction layer forms a Moiré-like height modulation structure that induces a row pattern running along [110]. There, the ridges (R) and the valleys (V) are formed with a distance of about 5 $|\mathbf{a}_q|$ above top and hollow positions, respectively. Due to the misfit between the atomic rows of the hex and the (1×1) square lattice, slight height modulations along the rows additionally occur where the hex atoms reside on bridge sites.

Figures 2(a) and 2(b) show atomically resolved STM images of the reconstructed Au(001) surface measured at 90 K. The characteristic row pattern running along [110] can be clearly perceived. The rows periodically display a characteristic splicing. In addition, there are also the expected small height modulations along the rows. However, additional large scale modulations in height, which are visible in Fig. 2(b), reveal that a simple square (5×20) or (5×28) cell, as indicated by black rectangles, is unsuited for characterizing the formed superstructure. Obviously, one needs a much larger unit cell having a rhombic shape which can be described by a centered rectangle, as displayed in red in Fig. 2(b). This becomes more obvious from Fig. 3 showing a larger area of the sample. It consists of three terraces that are marked as 1, 2, and 3 ascending from left to right and separated by atomic steps. In Fig. 3(a), the STM contrast is maximized for the largest terrace 3. Besides the characteristic pattern of the almost fivefold periodic reconstruction rows running along [110], one observes darker appearing areas of slight depressions that form a well-defined rhombic lattice. Its unit cell is indicated by red dashed lines. The insets show the fast Fourier transform (FFT) of the observed rhombic superstructure. Together with the innermost spots of the almost fivefold periodicity (encircled),

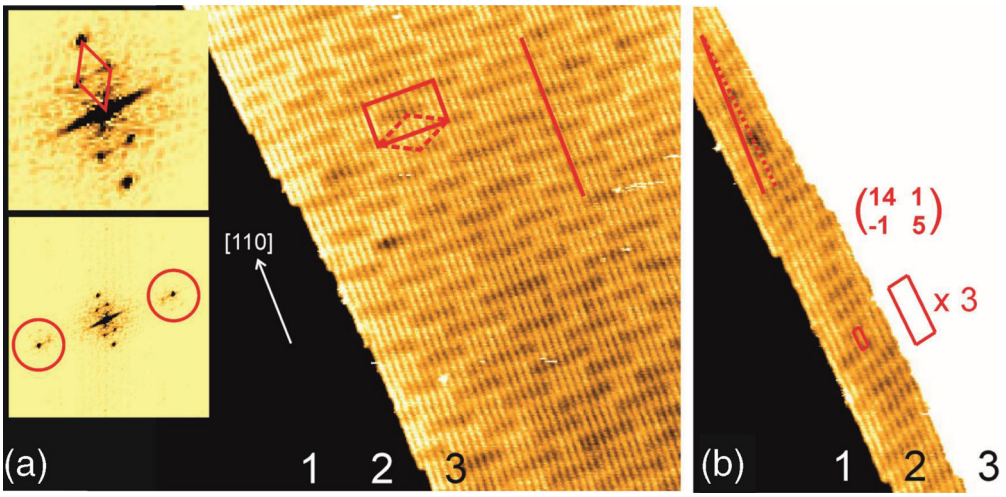

FIG. 3. (Color online) (a) and (b) STM images (500 pA, 1.0 V) of a stepped area of the Au(001)-hex showing three terraces 1, 2, and 3. Image contrast is maximized in (a) for terrace 3 (image size 150 × 108 nm^2) and in (b) for terrace 2. Weak depressions appearing in (a) in a darker contrast display a $c(2m \times 2n)$ superstructure as indicated by red diamond and rectangle. From the FFT patterns (insets) a $c(28 \times 48)$ structure has been deduced. For the narrow terrace 2, a slight rotation of the reconstruction rows is obvious which indicates that a $\begin{pmatrix} 14 & 1 \\ -1 & 5 \end{pmatrix}$ superstructure is possibly present.

it clearly reveals spots of the reciprocal rhombic superstructure marked in the upper, enlarged FFT.

A rhombic superstructure can be described by a rectangular centered $c(2m \times 2n)$ unit cell [shown in Fig. 3(a) by red solid lines] which is defined by the vectors $\mathbf{a}_l$ and $\mathbf{a}_s$ representing its long and short side, respectively. Their relation to the Au(001) square lattice is given by

$$|\mathbf{a}_s|/|\mathbf{a}_q| = m, \quad |\mathbf{a}_l|/|\mathbf{a}_q| = n, \quad \text{and} \quad |\mathbf{a}_s|/|\mathbf{a}_l| = m/n. \tag{1}$$

Correspondingly, in the reciprocal space one obtains

$$|\mathbf{b}_s|/|\mathbf{b}_q| = 1/n, \quad |\mathbf{b}_l|/|\mathbf{b}_q| = 1/m, \quad \text{and}$$
$$|\mathbf{b}_s|/|\mathbf{b}_l| = m/n. \tag{2}$$

From the lengths b_l and b_s of the reciprocal unit cell as determined from the FFT [see insets of Fig. 3(a)], the values m and n can be estimated. Using the spots of the almost fivefold periodicity as calibration markers with their distance $b_{1/5}$ to (0,0) $\approx 1/5\ |\mathbf{b}_q|$ one obtains with $5\ b_{1/5}/b_l \approx m$ and $5\ b_{1/5}/b_s \approx n$ value ranges of $13 < m < 15$ and $22 < n < 26$.

For a commensurate $c(2m \times 2n)$ superstructure, the diffraction spots of the Au(001)-hex are related to the reciprocal lattice of the Au(001) substrate in terms of rational numbers. For this specific case, as Van Hove *et al.* [21] pointed out, m and n are integers and the relations

$$b_{1/5} = (n' + 1)b_s \quad \text{and} \quad n = 5n' + 4 \tag{3}$$

hold where n' is also an integer. Within the experimental accuracy of the FFT, only an integer value of $n' = 4$ is possible. Hence, under the assumption of a commensurate hex layer, a $c(28 \times 48)$ superstructure of the Au(001)-hex can be deduced for the terrace 3 imaged in Fig. 3(a), which only slightly deviates from the $c(26 \times 48)$ observed by Binnig *et al.* [38].

In the direct neighborhood of the large terrace 3, the narrow terrace 2 is located. Its STM contrast is maximized in Fig. 3(b). Instead of the rhombic depression pattern, one observes there a stripelike one. In addition, the characteristic reconstruction rows appear slightly rotated. Comparing the [110] orientation of the reconstruction rows of terrace 3 (indicated by solid red lines) with the row orientation of terrace 2 (indicated with a dotted red line), one observes a deviation of about 4°. A similar rotation of the reconstruction rows was reported in former studies for stepped Au(001) samples [34] where it has been explained by a hex layer rotation of 0.7° yielding a $\begin{pmatrix} 14 & 1 \\ -1 & 5 \end{pmatrix}$ superstructure having a rhomboid unit cell. This structure also explains the stripelike depression pattern as the indicated unit cell visualizes.

The analysis of STM images as in Fig. 3 demonstrates a general problem of high-resolving, but locally restricted, probes such as STM. On the one hand, one can size the given structures very precisely. On the other hand, one is never sure whether the observed structure is representative for the whole sample or whether it is modified by local defects such as steps.

Applying high-resolution SPA-LEED in combination with a sample of high structural perfection may circumvent this restriction. In Fig. 4(a), a SPA-LEED image of the reconstructed Au(001) is shown. It demonstrates the high resolution power of the method by a narrow half width of the diffraction spot of about 0.8% of the Brillouin zone length. Note that all diffraction spots including the (0,0) spot are accessible since shadowing effects due to the sample holder or the electron gun do not arise. The reciprocal unit vectors $\mathbf{b}_{1,2q}$ of the (1×1) square lattice substrate and $\mathbf{b}_{1,2h}$ of the hex layer are drawn in Fig. 4(a) as black and red arrows, respectively. The dashed red arrows indicate that two domains of the hex layer exist. In addition, one observes the characteristic groups of extra diffraction spots of the Au(001) reconstruction that appear roughly at 1/5 order positions with respect to the Au(001) square lattice. Only weakly discernible in previous LEED investigations, they are now clearly resolved. They have V-, W-, diamondlike, or longer zigzaglike arrangements.

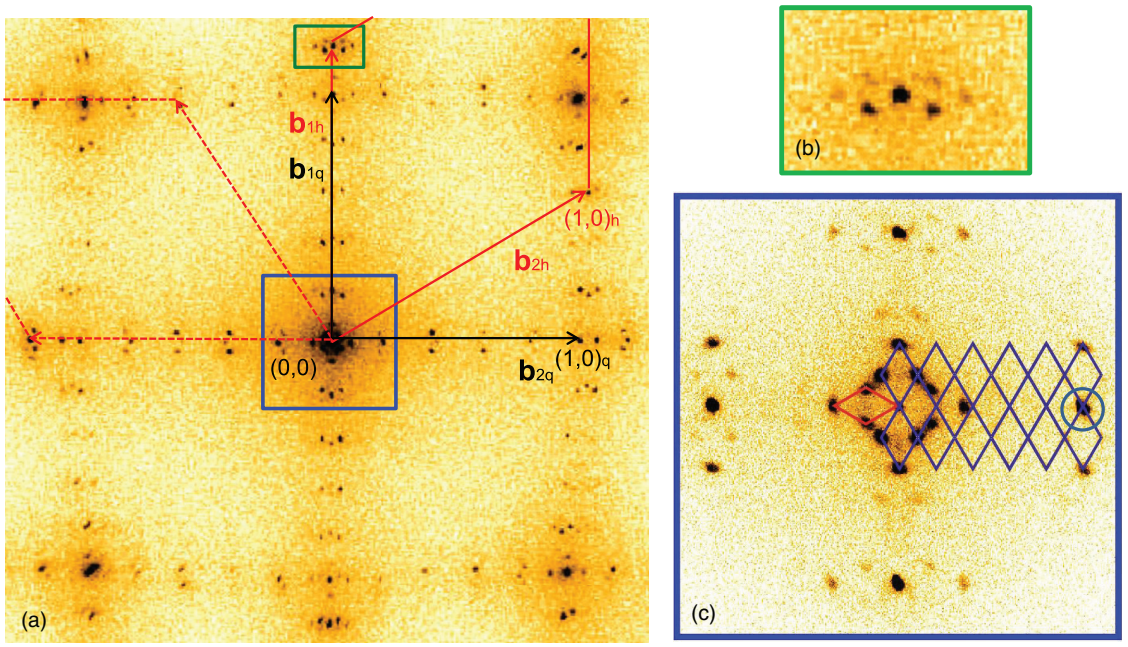

FIG. 4. (Color online) (a) SPA-LEED pattern of the Au(001)-hex taken at 220 eV. Reciprocal lattice vectors $\mathbf{b}_{1,2q}$ and $\mathbf{b}_{1,2h}$ of the Au(001) substrate square lattice and the hex layer on top, respectively, are indicated. (b) and (c) show the surroundings of the $(01)_h$ and the (00) spots measured at 220 and 190 eV, respectively. In (c), the blue and red diamonds visualize the unit cells of both hex domains. The red diamondlike network demonstrates for one domain the reciprocal Moiré-like lattice of the quasihexagonal Au(001) reconstruction.

This immediately shows again that the Au(001) reconstruction cannot be described by a primitive rectangular unit cell such as the (5 × 20) one.

Inspecting the region where the first order spot of the hex layer is located [smaller green rectangle in Fig. 4(a), enlarged in Fig. 4(b)] one observes that vector $\mathbf{b}_{1h}$ runs exactly along the direction of $\mathbf{b}_{1q}$ to the sharp $(0,1)_h$ spot. Correspondingly, the hex layer is present here in its nonrotated form with $\mathbf{a}_{1h}$ running exactly along [110]. Comparing the spot pattern around the (0,0) and the first order spots of the Au(001) square lattice, e.g. $(0,1)_q$, $(1,1)_q$, $(1,0)_q$, it becomes obvious that they are arranged in a similar configuration. This is a strong signature of a commensurate matching between the hex layer and the square lattice of the Au(001) substrate. For a noncommensurate structure, these spot patterns would be different [59]. Measuring the surroundings of the (0,0) spot with higher resolution at 190 eV [large blue square in Fig. 4(a), enlarged in Fig. 4(c)], all close-lying spots around the (0,0) can be observed with a brilliant contrast. They define in high resolution the reciprocal unit cell of both domains of the Au(001) reconstruction. As indicated by blue and red lines in Fig. 4(c), the unit cell has a rhombic shape. Similar as for the single hex domain measured with STM [compare Fig. 3(a)], it can be also described by a $c(2m \times 2n)$ superstructure. As indicated in blue lines, the unit cell forms a rhombic lattice which perfectly coincides with all spot positions visible in the (0,0) surroundings for the corresponding domain. This is an additional indication for a commensurate $c(2m \times 2n)$ reconstruction. Hereby, it is notable that a fivefold sequence of the unit cell exactly matches the spots of the roughly 1/5 order positions [one is encircled in Fig. 4(c)]. This has been additionally proven by applying Gauss fit procedures for exact determination of the spot positions. From (i) the distance $b_{1/5}$ of the roughly 1/5 order spots to the (0,0) spot and (ii) the measured size of the unit cell with their long and short sides b_l and b_s, one directly gets via Eqs. (2) and (3) that $m = 14 \pm 0.2$ and $n = 24 \pm 0.3$. Hence, taking only the highly resolved diffraction pattern of the (0,0) surroundings, SPA-LEED yields a commensurate $c(28 \times 48)$ structure for the Au(001)-hex reconstruction measured with a precision of about 1.5%.

For corroborating this finding, we have analyzed to which accuracy the $c(28 \times 48)$ structure defines the positions of all the other diffraction spots, too. For this purpose a careful correction of the instrumental barrel distortion of the SPA-LEED images [56] had been applied as described above. In Fig. 5, the region along the (0,0) and $(0,-1)_q$ spots is displayed. Figure 5(a) shows the raw data, i.e. the distorted image. For the strongest spots visible in Fig. 5(b), the barrel-corrected positions are indicated by superimposed gray dots. In Figs. 5(c) and 5(d), these data are shown together with the extended Brillouin zone scheme for both superstructure domains (blue and red). The perfect match between all corrected spot positions and both superstructure nets confirms the $c(28 \times 48)$ structure indeed very precisely (better than 1%). Based on the analysis in Figs. 5(c) and 5(d), the assignment of each diffraction spot to one of the two rotational $c(28 \times 48)$ domains becomes evident. In summary, at 300 K the surface reconstruction of a perfect Au(001) sample induces a Moiré-like $c(28 \times 48)$ superstructure, which is in commensurate registry with the square lattice of the Au(001) substrate. The real space vectors $\mathbf{a}_{1,2h}$ of the hex layer are described by

$$\begin{aligned} &\mathbf{a}_{1,h} || \mathbf{a}_{1q}, \quad |\mathbf{a}_{1,h}| = 0.9655 |\mathbf{a}_q|, \\ &|\mathbf{a}_{2,h}| = 0.9581 |\mathbf{a}_q|, \quad \varphi(\mathbf{a}_{1h}, \mathbf{a}_{2h}) = 59.75^\circ, \end{aligned} \tag{4}$$

where $\varphi(\mathbf{a}_{1h},\mathbf{a}_{2h})$ is the angle between both hex vectors.

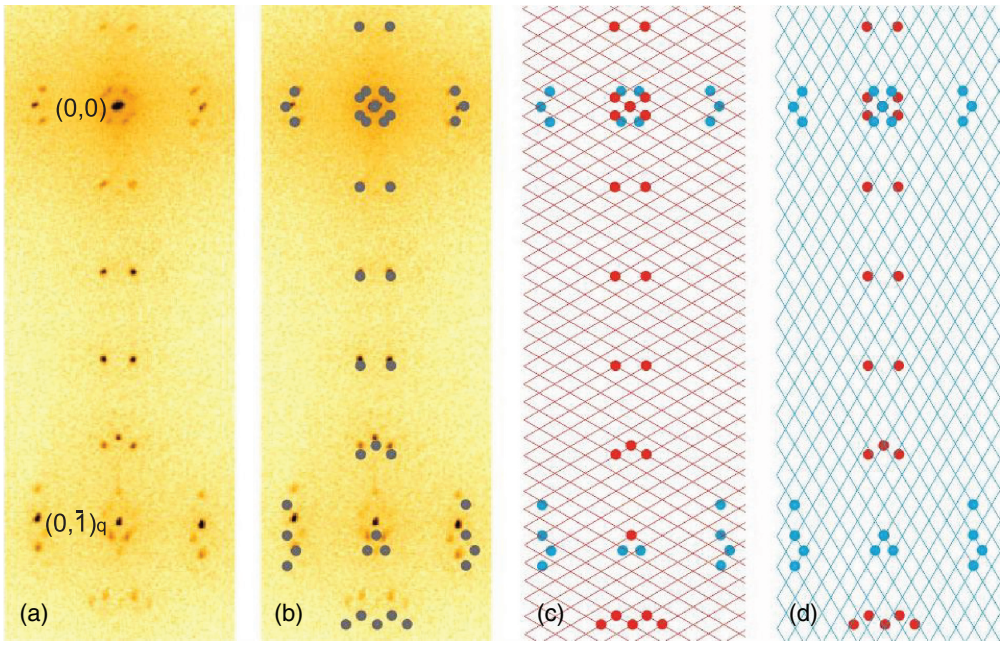

FIG. 5. (Color online) (a) Section of the SPA-LEED pattern of the Au(001)-hex as measured over the (00) and (0-1)$_q$ spot region of the Au(001) substrate square lattice. LEED energy 235 eV. (b) Same section with corrected spot positions given in gray dots. (c) and (d) Diamondlike networks shown in red and blue visualize the reciprocal Moiré-like lattice of both domains of the quasihexagonal Au(001) reconstruction. The corresponding LEED spots are taken from (b) and indicated in red and blue.

B. The rotated Au(001)-hex

In the second part of our investigation the rotation tendency of the hex layer, which has been observed in several previous studies, will be addressed. First, we followed former reports and applied annealing procedures for activating top layer rotation. However, within the investigated temperature range (300–1000 K), no indications of a top layer rotation was found for the used high-quality sample. Stimulated by reports on the influence of crystalline defects [5,34,39,44,50–54], Ar^+ sputtering at an elevated temperature of 650 K has been applied. At this temperature, sputtering induces only a slight distortion of the sample structure (e.g. via some Ar implantation). This is indicated in the LEED images by the (0,0), (0,1)$_q$, and (1,0)$_q$ spots of the square lattice Au(001) substrate. As visible in Fig. 6(a), they remain almost unchanged in sharpness and brilliancy (compare to Fig. 4). On the other hand, the LEED spots associated with the hexagonal reconstruction display now a clear linear blurring [see Figs. 6(a)–6(d)]. The blurring effect is most spectacular in the immediate neighborhood of the (0,0) spot. There, the spots of the rhombic $c(28 \times 48)$ superstructure are transformed to a crusaders crosslike pattern [compare Figs. 4(c) and 6(b)]. For the first order hex spots (0,1)$_h$ [Figs. 6(a) and 6(c)] and (1,0)$_h$ [Figs. 6(a) and 6(d)], one observes that the blurring appears bowlike on a circle around the (0,0) spot. This clearly indicates that the hex layer is now present in a slightly rotated form. In Fig. 6(e), the blurring is shown for the line scan measured over the (1,0)$_h$ spot. Using the profile of the sharp (1,0)$_q$ spot of the perfect surface [dotted curves in Fig. 6(e)], we estimate a maximum rotation angle of about $\pm 0.83° \pm 0.02°$. The continuous course of the blurring profile indicates a continuous distribution of rotation angles between the two extreme values. Note that also other Moiré spots (compare Fig. 7 below) support the continuous distribution of rotation angles. The rotation-induced blurring effect is almost identical for the (0,1)$_h$ and (1,0)$_h$ spots. Therefore, one can conclude that the changed diffraction pattern can be explained by a hex layer for which the internal structure is not changed during rotation.

To understand the sputter induced effects observed in SPA-LEED, we performed a simulation of the diffraction pattern by considering the Moiré-like modulation of the hex layer and its modification during hex layer rotation. This Moiré approach is based on the knowledge that the Fourier plane image of two periodic lattices, which form a Moiré pattern in real space, can be described by a convolution of two involved reciprocal lattices [60,61]. Following the Moiré approach the positions $\mathbf{b}_{m,n,m',n'}$ of the diffraction spots can be described by the sum of two reciprocal lattice vectors, one (m,n) for the square lattice of the substrate and one (m',n') for the hex top layer lattice

$$\mathbf{b}_{m,n,m',n'} = (m\mathbf{b}_{1q} + n\mathbf{b}_{2q}) + (m'\mathbf{b}_{1h} + n'\mathbf{b}_{2h}). \qquad (5)$$

In all simulations, we included an empirical *ad hoc* structure factor which describes well the decreasing intensity I with the diffraction order by

$$I = (m+n)^{-3}.$$

The simulation of the diffraction pattern for the nonrotated hex structure is shown in Fig. 7(a) in which the diffraction intensity is represented by gray levels. One observes that the Moiré approach leads to a very detailed agreement between the simulated and the measured diffraction pattern [compare Fig. 4(a)]. As observed in the measurement, only in the direct vicinity of the lines connecting $(0,m)$ and $(1,n)$ positions, spots appear with noticeable intensities similar for the corresponding domain. Figure 7(b) shows the diffraction area around the (0,0)

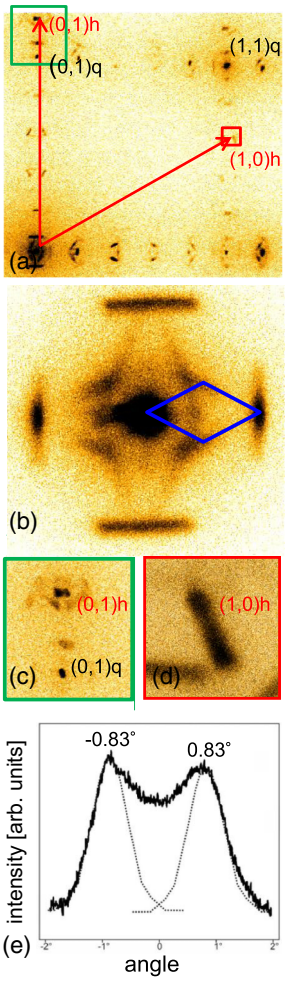

FIG. 6. (Color online) (a) Section of the SPA-LEED pattern of the rotated Au(001)-hex (upper right quadrant) with spots of the Au(001) substrate square lattice $[(0,1)_q, (1,1)_q, (1,0)_q]$ and of the hex $[(0,1)_h, (1,0)_h]$. (b)–(d) show vicinities of (0,0), $(0,1)_q$, and $(0,1)_h$, and $(1,0)_h$ spots, respectively. For comparison, the unit cell of the nonrotated Au(001)-hex is indicated by a blue diamond in (b). In (e), a line scan measured over the blurring of the $(1,0)_h$ spot is shown. The dotted curves visualize the spot shape of the sharp (0,1) spot. (a)–(c) LEED energy 220 eV, (d) and (e) 235 eV.

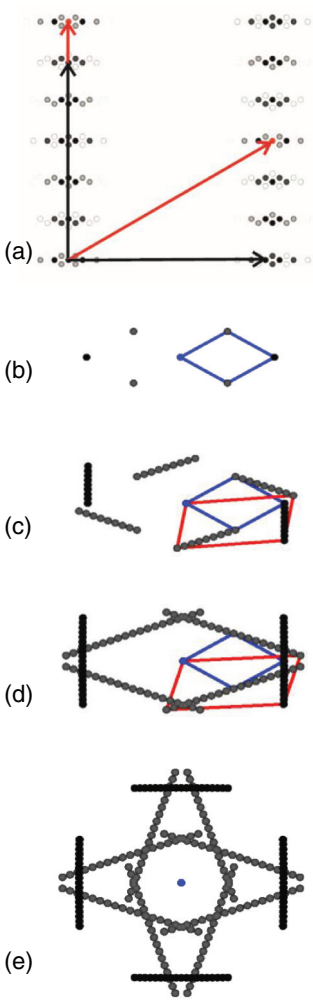

FIG. 7. (Color online) (a) Simulated diffraction pattern of one domain of the nonrotated Au(001)-hex (upper right quadrant). Reciprocal lattice vectors $\mathbf{b}_{1,2q}$ and $\mathbf{b}_{1,2h}$ of the Au(001) substrate square lattice and the hex layer on top are indicated in black and red, respectively. The surrounding of the (0,0) spot is shown in (b)–(e) for the nonrotated hex and for stages of a stepwise hex rotation. Rotation steps 0.05°, (c) rotation angles 0° to 0.4° and (d) 0 to ±0.85°. (e) Superposition of the simulated pattern of (d) with that of the corresponding other hex domain.

spot where the simulation yields the spots characterizing the $c(28 \times 48)$ unit cell (blue diamond).

For the simulation of the diffraction pattern of the rotated hex layer, we concentrate on the area around the (0,0) spot. Figure 7(c) shows the simulation obtained for eight clockwise rotation steps of the hex layer by $\alpha = 0.05°$ steps, i.e. for $\alpha = 0.00°$–$0.40°$, under the assumption that the internal lattice parameters stay as defined in Eq. (4). One can perceive that, during the hex layer rotation, the diffraction spots of the primitive unit cell move on almost linear courses. This indicates a drastic change of the large real space unit cell: it transforms to a rhomboid in reciprocal space. Figure 7(d) shows the situation obtained after 2×17 rotation steps including also the counterclockwise ones for $\alpha = 0.00° \pm 0.85°$. This angular range of rotations of the hex layer roughly characterizes the experimentally observed rotation range of angles up to ±0.83°. The superposition of both 90° domains finally yields a pattern [Fig. 7(e)] that fits perfectly the experimentally observed one shown in Fig. 6(b). Almost all details are reproduced in the simulation. Even the traces of the weaker spots formed during hex domain rotation which locally superimpose to higher intensities can be recognized. The experiment deviates only in one aspect, as both hex domains display an unequal rotation tendency. Whereas for one domain almost all rotation states between 0 and ±0.83° are realized, for the other low rotation angles are favored.

The traces of the unit cell spots due to the small angle rotations extend over a relatively long distance of about 8% of the Brillouin zone and reflect the hex layer rotation in a magnified manner. Their continuous progression indicates that there are no favorite rotation angles below 0.83°. The limiting rotational angle of 0.83° will be discussed later in the

context of a step interaction. Obviously, specific energetically favored locking places for the hex layer rotation do not exist. The excellent congruence between the measured and the simulated diffraction pattern is a strong argument for the validity of the initial assumption in the simulation, namely that the internal structure of the hex layer remains stable during rotation. This structural stability is certainly a result of the strong compression within the hex layer as it has been theoretically explained by the relativistically enhanced *d-d* hybridization [48,49].

The rotation of the hex layer can be turned back again simply by annealing the sample at temperatures around 90 K. During annealing, sputter-induced defects vanish and the high structural order of the sample is restored, which gradually reduces the degree of hex layer rotation. Correspondingly, the diffraction spots of stronger rotated domains continuously fade away as is shown in the sequence of SPA-LEED images displayed in Figs. 8(b) to 8(d) for increasing annealing temperatures. The sequence in Figs. 8(b) to 8(d) underlines the continuous character of the rotation angle distribution. At the end of this process, the original diffraction pattern of the nonrotated Au(001)-hex reappears [Fig. 8(d)].

C. Interaction between steps and Au(001)-hex

There is morphological evidence for the interaction of the hex layer with the steps of the Au(001) surface. As visible in Fig. 3, the steps show a clear trend to follow the direction of the reconstruction rows, and step edges are formed in their valley regions *V* (compare model of Fig. 1). This holds for rotated as well as nonrotated hex domains. Small angle deviations of the step edge direction are realized by the formation of kinks in the step edge having the width of the reconstruction rows. This reconstruction-induced step alignment has been revealed already in previous studies, e.g. for rough surfaces obtained after Ar ion bombardment [54] or for two-dimensional islands formed during homoepitaxial Au growth [18,62]. In the latter case, "magic" widths of reconstructed islands have been reported [62]. For vicinal Au(001), also magic areas have been observed, where the terrace widths are strongly related to the reconstruction period [51]. In addition, also an increase of the reconstruction period due to the stress field of the steps has been reported [5].

In this paper, we consider the general problem how the hex layer evolves from terrace to terrace over a step. First, we focus on the case of the nonrotated hex. For the interaction of the nonrotated $c(28 \times 48)$ hex layer with steps, three possible scenarios are imaginable: (i) the hex layer covers steps like a carpet, (ii) the hex reconstruction develops independently on different terraces, and (iii) the step structure is part of the hex reconstruction. For our high-quality Au(001) sample, [110] steps are dominating. There, the atoms of the step and of the hex layer are found close packed. In Fig. 9(a), a STM image with such a [110] step is displayed. Atomic rows of the hex layer are locally resolved. Here, [110] reconstruction rows with their periodic splicing are clearly perceivable. Interestingly, the step displays alternating kinks to the left and right, which yield a rectangular step course. This will be discussed below in more detail. In Fig. 9(b), the contrast of the lower (left) and upper (right) terraces visible in Fig. 9(a) is equalized. The

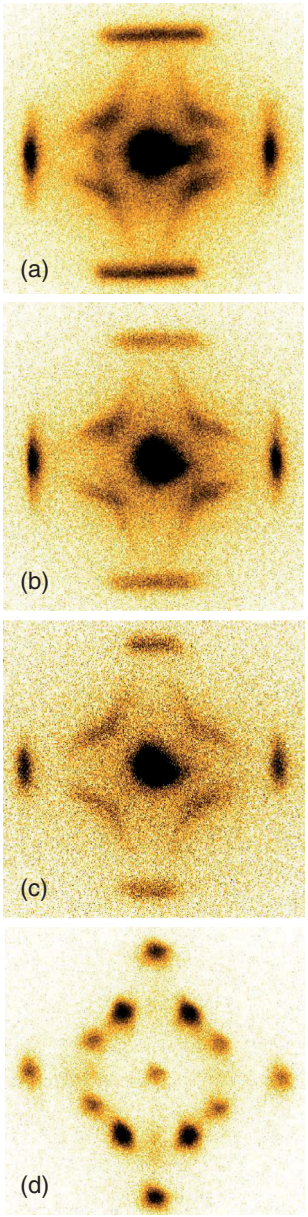

FIG. 8. (Color online) (a) SPA-LEED pattern of the vicinity of the (0,0) spot of the rotated Au(001)-hex and its change during annealing to (b) 870 K, (c) 920 K, and (d) 970 K. LEED energy 220 eV.

STM image shows that there is clearly no carpetlike behavior of the hex layer. On the one hand, the step has a sharp shape. On the other hand, there is a small, but clear lateral offset of the atomic rows running along [110] on two adjacent terraces. This is visualized by equidistant red lines lying on the right terrace on the atomic rows and on the left terrace between the atomic rows. A carpetlike hex layer would not show such an offset. Nevertheless, there is a clear interrelationship between the hex structures on both terraces. If one uses similar characteristic features of the $c(28 \times 48)$ hex structure, e.g. areas where the reconstruction rows are spliced [encircled in Fig. 9(c)], one can define the large Moiré unit cells on both terraces in an uniform manner as indicated by rectangles drawn in red. The obtained positions of the unit cells show that the lateral

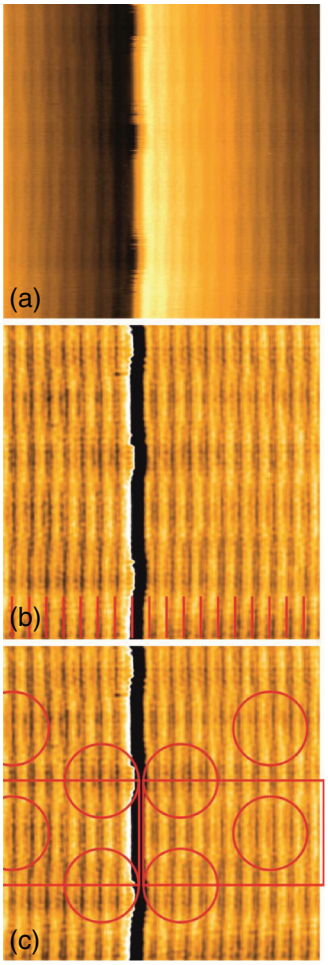

FIG. 9. (Color online) (a) STM image of the nonrotated Au(001)-hex with a [110] step (25 × 25 nm^2, 50 pA, 1.04 V). (b)–(c) Same STM image but with balanced contrast on both terraces. Equidistant lines in (b, bottom) run on the lower (left) terrace between atomic rows and on the higher (right) terrace on atomic rows. In (c), areas of reconstruction row splitting (encircled) are used for defining relative positions of the $c(28 \times 48)$ unit cell on both terraces.

displacement between the hex structures on both terraces is small along the steps ([110] direction). This observation allows a deeper understanding of the relationship between the step and the reconstruction structure as will be discussed by means of the hard sphere models of the $c(28 \times 48)$ reconstruction in Fig. 10. There the Au(001) substrate is represented by gray circles showing a smooth atomic step running straight along [110]. On the left terrace, which is one atomic step lower than the right terrace, a nonrotated $c(28 \times 48)$ hex layer (drawn in red) is superimposed. The hex layer was constructed by using its lattice vectors defined by Eq. (4). It has been oriented on the substrate in such a way that close packed atomic rows are running along [110] and that a closest contact with the step atoms of the substrate square lattice is attained as can be seen on the enlarged scale in Fig. 10(b). The full $c(28 \times 48)$ unit cell is marked by the black rectangle in Fig. 10(a). For its definition, the hex atoms residing in the hollow positions of the Au(001) substrate square lattice have been arbitrarily chosen. Although very simple, the model mimics essential features of the $c(28 \times 48)$ reconstruction. Similar to the STM images, areas where the hex atoms occupy substrate hollow positions appear darker whereas atoms in top positions appear lighter. Hence, the reconstruction rows running parallel to the steps appear in a light/dark contrast. The characteristic splicing of the reconstruction rows is also reproduced by the model. It is now obvious that the splicing effect is induced by the periodic transitions of the hex atoms from hollow or top positions to saddle positions along the [110] direction, which is induced by the structural misfit to the substrate square lattice. Based on the models in Figs. 10(c)–10(e), we will discuss the continuation of the hex reconstruction across [110] steps of the substrate. In Fig. 10(c), the upper right terrace is covered by a nonrotated hex layer drawn in magenta. It is arranged in such a way that the atoms in the hex layer that are next to the step reside on hollow or bridge positions of the upper step edge. By this definition, the relative shift along the step edge direction between the hex layers on both terraces is not fixed. Hence, the mismatch along [110] of both hex structures may adopt all values between 0 and $28|\mathbf{a}_q|$, the short length of the $c(28 \times 48)$ unit cell. As this obviously is not experimentally observed by STM [see Fig. 9(c)], one has to withdraw the assumption of an independent development of the hex layer on both terraces.

We consider now the case where the step itself is part of the hexagonal reconstruction. In principle, two regular constellations are possible: An A-type step where the step forms a (100) microfacet with a rectangular arrangement of atoms, and a B-type step with (111) microfacets of triangular atomic arrangement. Both cases are shown with the hard sphere model of the $c(28 \times 48)$ reconstruction in Figs. 10(d) and 10(e). For both step structures, a defined structural relationship is determined between the domains on both terraces. For the A-type step, the lateral offset is about 14 $|\mathbf{a}_q|$ which is half the length of the small side of the $c(28 \times 48)$ unit cell. For the B-type step, however, the offset is almost negligible and amounts to 0.5 $|\mathbf{a}_q|$. Obviously, the latter case is just the situation that is experimentally observed [compare to Fig. 9(c)]. Hence, we conclude that steps are part of the hexagonal reconstruction and display a B-type configuration where atoms form a triangular arrangements. It can be rationalized by energetically favored (111) microfacets.

The simple hard sphere model of the step reconstruction yields also a plausible explanation of the alternating kink structure of the steps as revealed in the STM images [see Fig. 9(a)]. In Fig. 11(a), the hard sphere model of a straight reconstructed B-type step [as in Fig. 10(e)] is displayed in higher magnification. For the upper (right) terrace, the lower left part of the boundary of the $c(28 \times 48)$ unit cell is drawn in black similar as indicated in Fig. 10(e). Note that the left part of the boundary is defined by the upper step atoms. Considering the hex structure below the step, one perceives slight modifications having the periodicity of 28 $|\mathbf{a}_q|$ along [110]. The relative atomic positions are different at the corner region of the unit cell (marked by a green rectangle) and at the region half the periodicity further along the step [marked by the blue rectangle and shown enlarged in Fig. 11(b)]. For the latter, the threefold hollow positions of the hex near the step edge are located directly above an atom of the subjacent square lattice substrate (shown in gray). Hence, the atomic configuration resembles a regular hexagonal close-packed (hcp) site of a face-centered-cubic (fcc) (111) surface. At

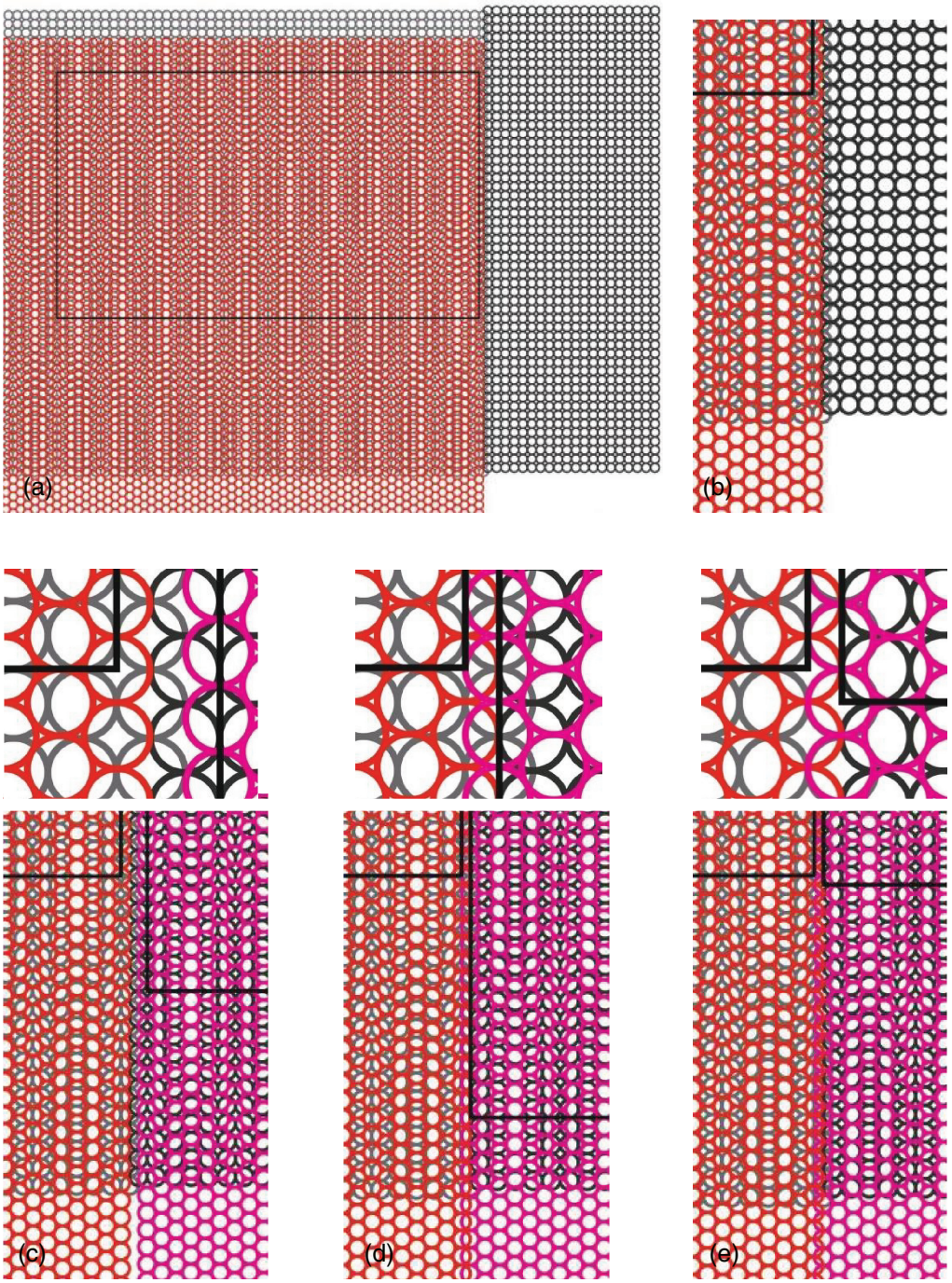

FIG. 10. (Color online) (a)–(e) Hard sphere models of the $c(28 \times 48)$ Au(001)-hex structure visualizing different step situations. (a) and (b) hex layer (atoms in red) on Au(001) substrate square lattice (atoms in gray), attached at the lower step side. Black rectangle indicates the $c(28 \times 48)$ unit cell. (c)–(e) show additionally the hex layer at the upper step side (atoms in magenta) for (c) independent terrace population and for hex layers with (d) A-type and (e) B-type steps. For explanations, see text.

the corner region [green square in Fig. 11(a) and enlarged in Fig. 11(c)], however, the hollow positions are situated above bridge positions of the subjacent substrate square lattice. These different substructures should imply different bonding energies for atoms diffusing along or arriving at the step [shown in yellow in Figs. 11(b) and 11(c)]. Assuming the more regular hcp site as the place of stronger bonding, an incoming atom would not only be captured there, but it would also define two kink sites that would act as very effective traps for other diffusing atoms. Hence, around the hcp site a one-dimensional chain of atoms will form. At the same time, step sites near the "corner" positions may stay unoccupied due to their weaker bonding strength. As a consequence, the step develops an alternating kink pattern with 28 $|\mathbf{a}_q|$ periodicity just as observed in the STM measurements [compare Figs. 9(a) and 9(d)].

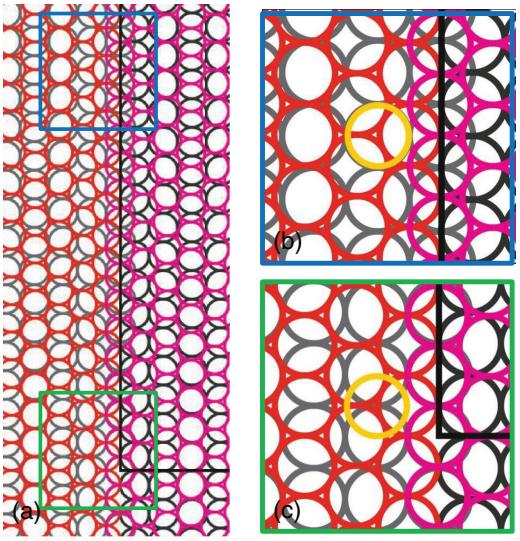

FIG. 11. (Color online) (a)–(c) Hard sphere model of the $c(28 \times 48)$ Au(001)-hex with B-type step structure. Same situation as shown in Fig. 10(e). (b) and (c) visualize the structural situation for atoms in step sites (displayed in yellow) in different step areas as indicated by blue and green squares.

As a last issue, we discuss the local [110] step structure for the rotated hex layer. Figures 12(a) and 12(b) show STM images of a step within a rotated hex area which reveal a clearly modified surface structure as compared to the previously discussed nonrotated hex layer. Most strikingly, the step structure now shows a stairway propagation. Instead of alternating atomic kinks to the left and to the right, there are only kinks to one side. As the kinks are arranged approximately periodically, the step contour appears inclined by a well-defined angle of about 4.5° with respect to the [110] direction. In the STM images, one also recognizes the characteristic reconstruction rows that again run parallel to the step. In contrast to the nonrotated hex layer, they are rotated similar as the steps by an angle of about 4.5°. Note the slight height modulations along the rows. They exhibit a distinct displacement between neighboring rows. Connecting corresponding positions of maxima or minima, one obtains lines [one is dotted in Fig. 12(b)] which are inclined to the [110] direction by about 22°.

The simple hard sphere model of the Au(001) reconstruction again allows a straightforward explanation of these observations. Figure 12(c) shows the model of a rotated step with atomic kinks to the left. At the lower terrace, a hex layer with $c(28 \times 48)$ structure is constructed according to Eq. (4), with close-packed atomic rows rotated with respect to the [110] direction counterclockwise by 0.83°, the maximum rotation angle as measured by LEED (Fig. 6). Areas where the hex atoms occupy hollow positions of the substrate appear darker in the model as well as in the STM image, whereas atoms in top positions appear brighter. The characteristic long-range

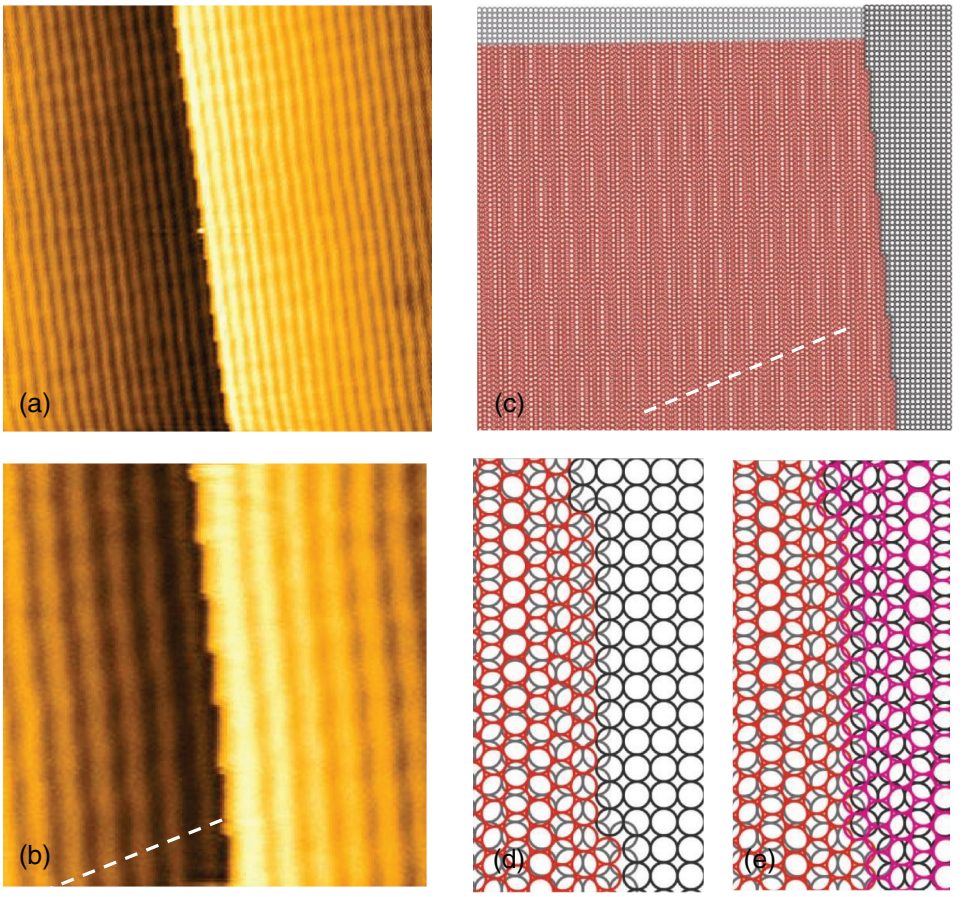

FIG. 12. (Color online) (a) and (b) STM images (50 pA, −0.98 V) and (c)–(e) sphere models of the rotated Au(001)-hex in step vicinity. STM image sizes (a) 45×45 nm^2 and (b) 18×18 nm^2. For explanation, see text.

reconstruction rows are now rotated by about 4.5° with respect to the [110] direction, which nicely corresponds to the STM measurements of Figs. 12(a) and 12(b). In addition, one observes slight height modulations along the reconstruction rows. They show defined displacements from row to row similar to the STM measurements. Connecting neighboring positions of maxima or minima, one obtains lines (one is shown dotted) that are inclined to [110] by about 22° just as observed in the STM measurement [compare Fig. 12(b)]. The specific rotation angle of the step has been chosen according to the angle of the rotated reconstruction rows. As the latter is 4.5°, it can be realized by periodic kinks having a distance of $n\,|\mathbf{a}_q|$ with $n = 12$–13. The step rotation angle is 4.76° for $n = 12$, and 4.40° for $n = 13$. For the step in the model of Fig. 12(c), a kink distance of 12 $|\mathbf{a}_q|$ has been used. For the hex layer, this corresponds to a kink every 13 $|\mathbf{a}_{1,\mathrm{hex}}|$ and allows a close contact to the substrate step as shown in the magnification in Fig. 12(d). The kinks of the hex layer are almost perfectly interlocked with the kinks of the step of the square lattice substrate. Hereby, the hex atoms having the closest contact to the substrate ones are alternately found in near fourfold hollow positions and in near bridge positions of the substrate. In Fig. 12(e), the hex layer of the upper terrace (shown in magenta) is added. For the step atoms again a B-type situation [local (111) microfacets] is realized similar to that shown for the nonrotated step. At the step edge, the hex atoms of the upper terrace are also located in almost fourfold hollow positions or in almost bridge positions. The model, certainly, simplifies the actual situation. In reality, the kink distance is less well defined. From STM measurements such as shown in Fig. 12(b), one can derive kink distances $w\,|\mathbf{a}_q|$ with values of w fluctuating between 11 and 14. Finally, we have to stress that, only for the experimentally observed largest rotation angle of $\alpha = \pm 0.83°$, an almost perfect locking of the hex layer into the kink structure of the substrate step is attained as visualized in the model of Fig. 12(d). Larger rotation angles would require clearly less favored atomic step configurations. Probably this may be one of the reasons that the hex layer rotation stops at $\alpha = \pm 0.83°$.

IV. SUMMARY AND CONCLUSIONS

By using a single crystal of high structural perfection and combining the high-resolution power of STM and SPA-LEED, the Au(001) quasihexagonal reconstruction of the top layer has been determined with high precision. A well-developed $c(28 \times 48)$ structure has been determined, which is in commensurate registry with the square lattice of the substrate and corresponds to a nonrotated hex layer with close-packed atomic rows along the [110] direction. An additional rotation of the hex layer could be initiated by mild high-temperature sputtering. Rotation proceeds continuously up to angles of ±0.83° without strongly favored rotation angles. During rotation, the internal structure of the $c(28 \times 48)$ hex layer is maintained. This may be explained by the strong compression within the hex layer, which laterally stabilizes the hex lattice. Applying a Moiré approach, the complicated diffraction pattern of the rotated hex layer could be precisely simulated. The sputtering-induced rotation of the hex layer is found to be reversible upon annealing. For annealing temperatures around 900 K, a complete restoration of the nonrotated $c(28 \times 48)$ structure is found. The detailed local step structure, which is different for the rotated and the nonrotated hex layer, has been determined by STM and is rationalized in a simple reconstruction model. In both cases of reconstruction, atoms at the steps form a triangular B-type configuration where a (111) microfacet is present. The reconstruction model leads to a periodically varying bonding along the [110] step which explains the experimentally observed rectangular step structure. The reconstruction model allows one also to understand the 4.5° inclination of the step edge direction with respect to the [110] direction, which is observed within completely rotated hex layers. In this case, a regular kink structure is established along the step edge for the maximum rotation angle, which is explained by an optimized matching. This ideal matching situation is only found for rotation angles around ±0.83° which might explain that larger rotation angles are not realized.

ACKNOWLEDGMENTS

Financial support by the DFG Sonderforschungsbereich SFB-762, "Functionality of Oxidic Interfaces" and the DFG Sonderforschungsbereich SFB/TRR-102, "Polymers under Multiple Constraints" is gratefully acknowledged. The authors would like to thank R. Kulla for technical support.

[1] G. C. Bond, C. Louis, and D. T. Thompson, *Catalysis by Gold* (Imperial Collage Press, London, 2006).
[2] H.-J. Freund and G. Pacchioni, Chem. Soc. Rev. **37**, 2224 (2008).
[3] D. M. Kolb, Prog. Surf. Sci. **51**, 109 (1996).
[4] C. A. Lucas, P. Thompson, M. Cormack, A. Brownrigg, B. Fowler, D. Strmcnik, V. Stamenkovic, J. Greeley, A. Menzel, H. You, and N. M. Markovic, J. Am. Chem. Soc. **131**, 7654 (2009).
[5] M. Moiseeva, E. Pichardo-Pedrero, G. Beltramo, H. Ibach, and M. Giesen, Surf. Sci. **603**, 670 (2009).
[6] T. A. Green, Gold Bulletin **40**, 105 (2007).
[7] B. Voigtländer, G. Meyer, and N. M. Amer, Phys. Rev. B **44**, 10354 (1991).
[8] O. Fruchart, M. Klaua, J. Barthel, and J. Kirschner, Phys. Rev. Lett. **83**, 2769 (1999).
[9] M. Kiel, K. Duncker, C. Hagendorf, and W. Widdra, Phys. Rev. B **75**, 195439 (2007).
[10] A. Höfer, K. Duncker, M. Kiel, S. Wedekind, and W. Widdra, Phys. Rev. B **83**, 075414 (2011).
[11] K. Marre and H. Neddermeyer, Surf. Sci. **287-288**, 995 (1993).
[12] C. A. Ventrice Jr., T. Bertrams, H. Hannemann, A. Brodde, and H. Neddermeyer, Phys. Rev. B **49**, 5773 (1994).
[13] I. Sebastian, M. Heiler, K. Meinel, and H. Neddermeyer, Appl. Phys. A **66**, S525 (1998).
[14] K. Meinel, M. Huth, H. Beyer, H. Neddermeyer, and W. Widdra, Surf. Sci. **619**, 83 (2014).

[15] K. Meinel, M. Klaua, and H. Bethge, Ultramicroscopy **20**, 261 (1986).
[16] K. Meinel, M. Klaua, and H. Bethge, J. Chryst. Growth, **89**, 447 (1988).
[17] M. G. Goldiner, V. B. Sapozhnikov, M. Klaua, and K. Meinel, J. Phys.: Condens. Matter **3**, 5479 (1991).
[18] S. Günther, E. Kopatzki, M. C. Bartelt, J. W. Evans, and R. J. Behm, Phys. Rev. Lett. **73**, 553 (1994).
[19] M. Labayen, C. Ramirez, W. Schattke, and O. M. Magnussen, Nat. Mater. **2**, 783 (2003).
[20] A. Trembulowicz, G. Ehrlich, and G. Antczak, Phys. Rev. B **84**, 245445 (2011).
[21] M. A. Van Hove, R. J. Koestner, P. C. Stair, J. P. Biberian, L. L. Kesmodel, I. Bartos, and G. A. Somorjai, Surf. Sci. **103**, 189 (1981).
[22] J. V. Barth, H. Brune, G. Ertl, and R. J. Behm, Phys. Rev. B **42**, 9307 (1990).
[23] W. Moritz and D. Wolf, Surf. Sci. **88**, L29 (1979).
[24] T. Gritsch, D. Coulman, R. J. Behm, and G. Ertl, Surf. Sci. **257**, 297 (1991).
[25] D. G. Fedak and N. A. Gjostein, Phys. Rev. Lett. **16**, 171 (1966).
[26] D. G. Fedak and N. A. Gjostein, Surf. Sci. **8**, 77 (1967).
[27] R. F. Schlier and H. E. Farnsworth, J. Chem. Phys. **30**, 917 (1959).
[28] K. Takayanagi, Y. Tanishiro, S. Takahashi, and M. Takahasi, Surf. Sci. **164**, 367 (1985).
[29] W. Telieps and E. Bauer, Surf. Sci. **162**, 163 (1985).
[30] E. Bauer, A. K. Green, and K. M. Kunz, Appl. Phys. Lett. **8**, 248 (1966).
[31] P. W. Palmberg and T. N. Rhodin, Phys. Rev. **161**, 586 (1967).
[32] D. M. Zehner, B. R. Appleton, T. S. Noggle, J. W. Miller, J. H. Barret, L. H. Jenkins, and E. Schow, J. Vac. Sci. Technol. **12**, 454 (1975).
[33] F. Grønlund and P. E. Høilund Nielsen, J. Appl. Phys. **43**, 3919 (1972).
[34] H. Melle and E. Menzel, Z. Naturforsch. **33a**, 282 (1978).
[35] K. H. Rieder, T. Engel, R. H. Swendsen, and M. Manninen, Surf. Sci. **127**, 223 (1983).
[36] G. E. Rhead, J. Phys. F: Met. Phys. **3**, L53 (1973).
[37] J. F. Wendelken and D. M. Zehner, Surf. Sci. **71**, 178 (1978).
[38] G. K. Binnig, H. Rohrer, C. Gerber, and E. Stoll, Surf. Sci. **144**, 321 (1984).
[39] K. Yamazaki, K. Takayanagi, Y. Tanishiro, and K. Yagi, Surf. Sci. 199 (1988).
[40] Y.-F. Liew and G.-C. Wang, Surf. Sci. **227**, 190 (1990).
[41] N. Wang, Y. Uchida, and G. Lehmpfuhl, Surf. Sci. Lett. **284**, L419 (1993).
[42] N. Wang, Y. Uchida, and G. Lehmpfuhl, Surf. Sci. Lett. **296**, L1 (1993).
[43] D. Gibbs, B. M. Ocko, D. M. Zehner, and S. G. J. Mochrie, Phys. Rev. B **42**, 7330 (1990).
[44] J. de la Figuera, M. A. González, R. García-Martínez, J. M. Rojo, O. S. Hernán, A. L. Vázquez de Parga, and R. Miranda, Phys. Rev. B **58**, 1169 (1998).
[45] G. Ritz, M. Schmid, P. Varga, A. Borg, and M. Rønning, Phys. Rev. B **56**, 10518 (1997).
[46] F. Ercolessi, E. Tosatti, and M. Parrinello, Phys. Rev. Lett. **57**, 719 (1986).
[47] B. W. Dodson, Phys. Rev. B **35**, 880 (1987).
[48] N. Takeuchi, C. T. Chan, and K. M. Ho, Phys. Rev. B **43**, 14363 (1991).
[49] P. Havu, V. Blum, V. Havu, P. Rinke, and M. Scheffler, Phys. Rev. B **82**, 161418(R) (2010).
[50] W. Telieps, M. Mundschau, and E. Bauer, Surf. Sci. **225**, 87 (1990).
[51] Y. Samson, S. Rousset, S. Gauthier, J. C. Girard, and J. Klein, Surf. Sci. **315**, L969 (1994).
[52] D. N. Dunn, J. P. Zhang, and L. D. Marks, Surf. Sci. **260**, 220 (1992).
[53] Z. Gai, Y. He, X. W. Li, J. F. Jia, and W. S. Yang, Surf. Sci. **365**, 96 (1996).
[54] M. A. González, J. de la Figuera, O. Rodríguez de la Fuente, and J. M. Rojo, Surf. Sci. **429**, L486 (1999).
[55] U. Scheithauer, G. Meyer, and M. Henzler, Surf. Sci. **178**, 441 (1986).
[56] F. Sojka, M. Meissner, C. Zwick, R. Forker, and T. Fritz, Rev. Sci. Instrum. **84**, 015111 (2013).
[57] S. Förster, Ph.D. thesis, Martin-Luther-Universität Halle-Wittenberg, Halle, 2011.
[58] T. Matsumoto, M. Batzill, S. Hsieh, and B. E. Koel, Surf. Sci. **572**, 146 (2004).
[59] C. Ammer, K. Meinel, H. Wolter, A. Beckmann, and H. Neddermeyer, Surf. Sci. **375**, 302 (1997).
[60] O. Bryngdahl, J. Opt. Soc. Am. **64**, 1287 (1974).
[61] I. Amidror, *Volume I: Periodic Layers* (Springer, London, 2009).
[62] M. Nomura and X.-Q. Wang, Phys. Rev. Lett. **81**, 2739 (1998).